www.sciencemag.org/cgi/content/full/science.1224768/DC1

Supplementary Materials for

Jet-Launching Structure Resolved Near the Supermassive Black Hole in M87

Sheperd S. Doeleman,* Vincent L. Fish, David E. Schenck, Christopher Beaudoin, Ray Blundell, Geoffrey C. Bower, Avery E. Broderick, Richard Chamberlin, Robert Freund, Per Friberg, Mark A. Gurwell, Paul T. P. Ho, Mareki Honma, Makoto Inoue, Thomas P. Krichbaum, James Lamb, Abraham Loeb, Colin Lonsdale, Daniel P. Marrone, James M. Moran, Tomoaki Oyama, Richard Plambeck, Rurik A. Primiani, Alan E. E. Rogers, Daniel L. Smythe, Jason SooHoo, Peter Strittmatter, Remo P. J. Tilanus, Michael Titus, Jonathan Weintroub, Melvyn Wright, Ken H. Young, Lucy Ziurys

*To whom correspondence should be addressed. E-mail: sdoeleman@haystack.mit.edu

Published 27 September 2012 on *Science* Express
DOI: 10.1126/science.1224768

This PDF file includes:

Methods
Figs. S1 to S4
Tables S1 and S2
References (*37*–*41*)

Supplementary Materials:

Figures S1-S4

Tables S1-S2

References (37-41)

Supplementary Materials:

Observations and Calibration

M87 was observed over the first half of the night on each of 2009 April 5-7, using an array consisting of the JCMT on Mauna Kea (J), the SMT in Arizona (S), and two dishes from the CARMA array in California (C and D). On the summit of Mauna Kea in Hawaii, the Submillimeter Array (SMA) housed the VLBI recording system and synthesized the Hydrogen Maser based VLBI frequency reference used at the JCMT. The observational setup and correlation for this observing campaign have been described in detail elsewhere (37). The baseline coverage of the observations over the three days is shown in Figure S1.

Once correlated using the Mark4 VLBI correlator at Haystack Observatory, the data were fringe-fit using a standard data reduction package developed at Haystack Observatory for high frequency VLBI data reduction (37-40). The data were first inspected to determine the coherence time, the time interval over which the VLBI signal can be coherently integrated. For 1.3mm wavelength this time is determined by atmospheric turbulence and typically ranges from 1-30 seconds. VLBI detections were determined through a 2-d search over interferometer delay and delay-rate. At each search grid-point the data for a VLBI scan were rotated to the proper delay and delay-rate, and the scan (typically 10 minutes) was segmented into smaller intervals corresponding to the coherence time of the atmosphere. For each baseline, these segments were noise de-biased and incoherently averaged. A fringe detection is signaled by a significant peak in incoherent signal to noise ratio in the search.

To convert the processed data to units of correlated flux density, the VLBI correlation coefficient for each baseline was multiplied by the geometric mean of the System Equivalent Flux Density (SEFD) of both antennas. Measured in Janskys (Jy), the SEFD is a product of antenna gain (Jy/K) and the opacity corrected system temperature (Tsys). For all three sites, Tsys was measured just prior to each ~10 minute VLBI scan using a vane calibration technique that corrects for the atmosphere. For the JCMT and SMT, antenna gains were determined from observations of planets at several points during the multiple day campaign, and the gains were observed to be stable. Relative gains for the two CARMA dishes were estimated using observations taken by CARMA in interferometric array mode before each VLBI scan, and the gains were then set to a common flux scale using planet scans at the end of each night. The results of this a-priori calibration of the VLBI amplitudes are shown in Figure S2.

Large scale (~arcsecond) structure due to the relativistic jet in M87 causes beating in the amplitudes on the short baseline between the two CARMA antennas. The jet structure was imaged using CARMA array calibration data taken before each VLBI scan, and the resulting map is shown in Figure S3. The total flux density of M87 measured with the CARMA array was 1.9 Jy, and the value measured at the Submillimeter Array was 1.97 Jy. We have adopted the SMA value and adjusted the flux density level in the large scale M87 image accordingly.

After the a-priori calibration, there were clear differences between amplitudes on the CARMA-CARMA (CD) VLBI baseline and the amplitudes expected from the CARMA image (Figure S3). These differences may be due to imperfect determination of antenna SEFD or pointing errors. These same errors cause amplitude variation between baseline pairs to the two CARMA dishes (e.g., SC and SD or JC and JD). Variations within each scan between the two observing bands are caused by instrumental differences in the signal paths at each antenna for each band.

These residual calibration errors and amplitude variation were corrected as described in previous work (37). After the gain-corrections are applied, the CD amplitudes track the model amplitudes (with signal to noise determined by averaging the high and low band CD detections together), and the SD and SC baseline amplitudes are averaged to a single value per VLBI scan (again with signal to noise determined by computing the weighted average). The effect of gain-correction on the JC, JD, and SJ baselines is minimal <5%).

The short CD baseline is sensitive to emission on arcsecond scales, and variations of 10% in the amplitudes on this baseline are due to beating between the bright core and "knot A", compact emission due to a shock in the jet 12 arcseconds downstream. The dropoff of ~1 Jy between the very short CD baseline and the SMT-CARMA baselines (SC and SD) is indicative of resolved jet structure on scales larger than $300\,\mu as$. A similar dropoff is seen with 7 mm VLBI where arrays with more telescopes are able to map the extended emission in the jet on these scales (17).

Circular Gaussian Fits

Results of Gaussian fits on each day of observations are shown in Table S1. Data on the long baselines between the geographically separated sites (CARMA, JCMT, SMTO) were fitted using weighted least-squares to a circular Gaussian model parameterized by the Full Width Half Maximum (FWHM) and the total flux density. Contours of χ^2 were used to determine the uncertainty in each parameter (Table S1).

Lensed Size of the Innermost Stable Circular Orbit for Arbitrary Black Hole Spin

The radius of the Innermost Stable Circular Orbit (ISCO) for a black hole of arbitrary spin is given (in units of M) by (41)

$$R_{ISCO} = M\left(3 + Z_2 \mp \left[(3 - Z_1)(3 + Z_1 + 2Z_2)\right]^{1/2}\right) \quad (1)$$

$$Z_1 = 1 + \left[(1 - a^2/M^2)^{1/3}\right]\left[\left(1 + a/M\right)^{1/3} + \left(1 - a/M\right)^{1/3}\right] \quad (2)$$

$$Z_2 = \left(3a^2/M^2 + Z_1^2\right)^{1/2} \quad (3)$$

The upper sign in Eq. 1 is used for prograde orbits and the lower sign used for retrograde orbits.

The last photon orbit in the equatorial plane for a black hole with arbitrary spin is given by

$$r_{\pm\gamma} = 2M\left\{1 + \cos\left(\frac{2}{3}\cos^{-1}(\mp a/M)\right)\right\} \quad (4)$$

In the equatorial plane, the apparent radius of the ISCO for an observer at infinity is given by (28)

$$R_a = \left(b_+ - b_-\right)/2 \quad (5)$$

where

$$b_{\pm} = \pm \begin{cases} R\left(\dfrac{R\sqrt{R^2 - 2MR + a^2} \mp 2aM}{R^2 - 2MR}\right) & \text{if } R > r_{\pm\gamma} \\ r_{\pm\gamma}\left(\dfrac{r_{\pm\gamma}\sqrt{r_{\pm\gamma}^2 - 2Mr_{\pm\gamma} + a^2} \mp 2aM}{r_{\pm\gamma}^2 - 2Mr_{\pm\gamma}}\right) & \text{if } R < r_{\pm\gamma} \end{cases} \quad (6)$$

Figure 3 in the main report shows the intrinsic ISCO size and the apparent ISCO size as a function of black hole spin both in the equatorial plane (equation 6) and looking down the axis of rotation of the black hole (through ray-tracing simulations).

Calibrated 1.3~mm VLBI Data

Table S2 contains all of the VLBI data used for the size analysis in this work.

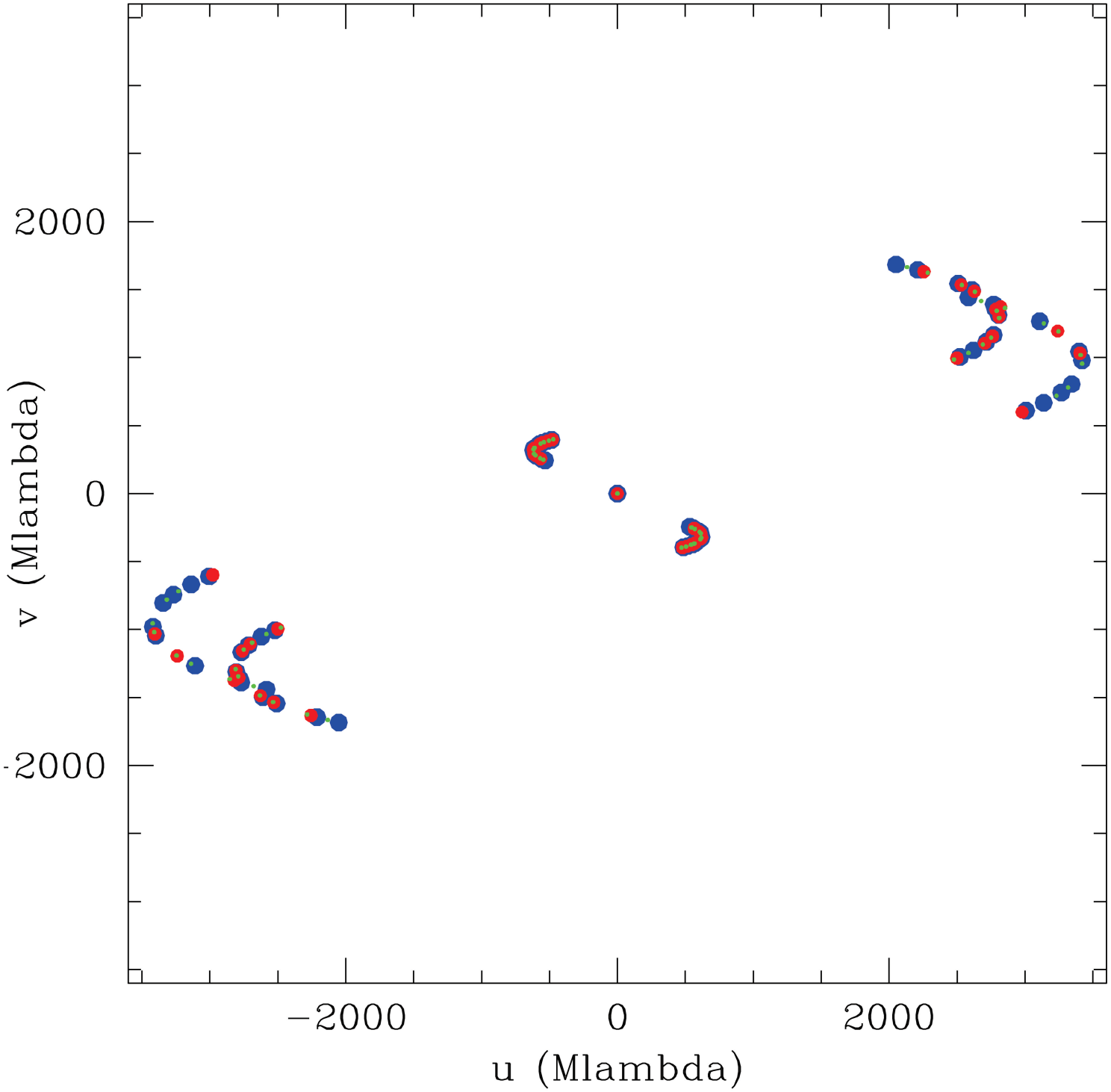

Fig S1. Baseline spacings for 1.3mm VLBI observations of M87 during nights of 2009 April 5, 6, and 7 (green, red, and blue points, respectively). The plot only shows (u,v) points for which M87 detections were obtained.

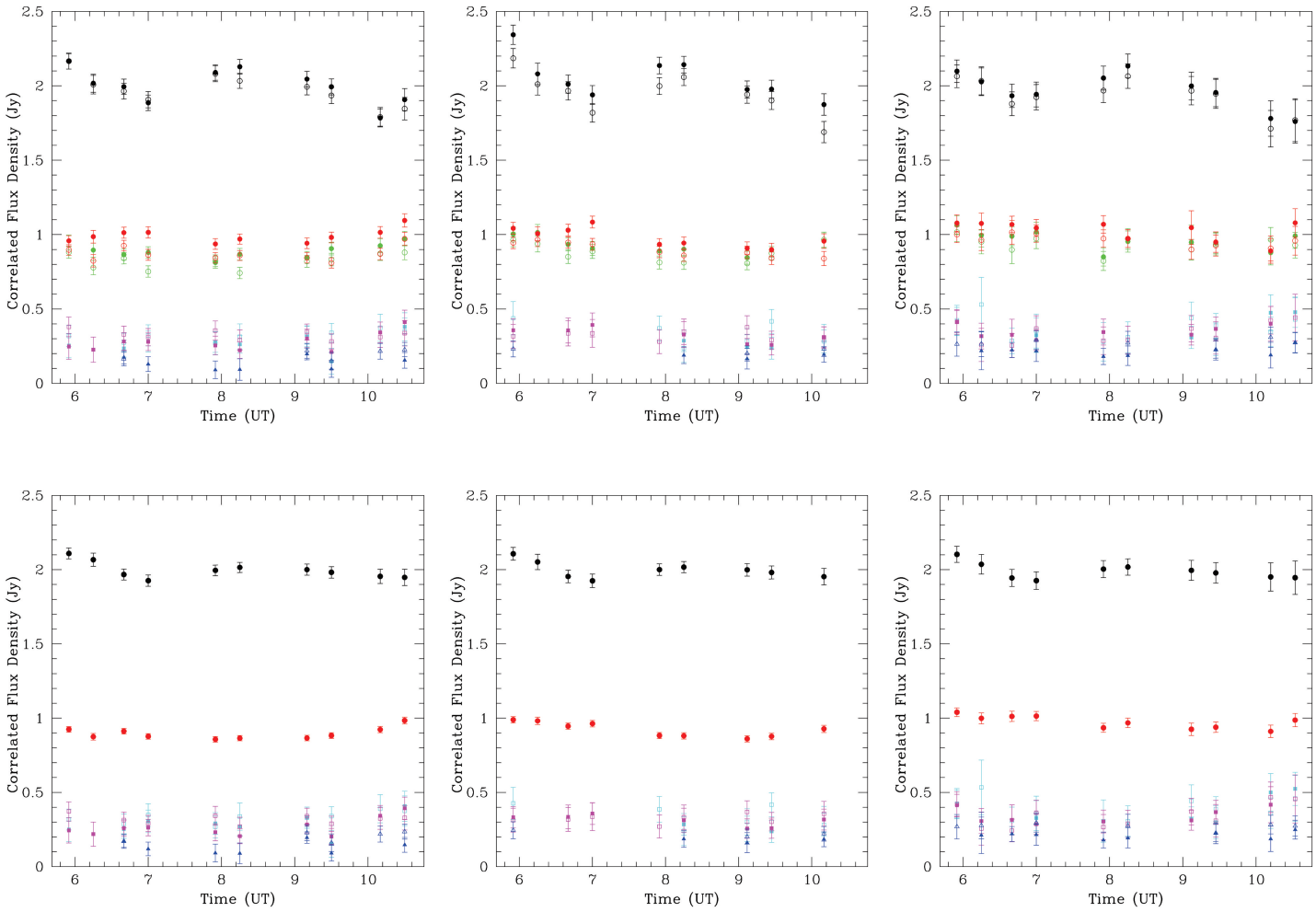

Fig S2. Top: A-priori calibrated visibility amplitudes of M87 as a function of time. Open symbols are data from the low band, and filled symbols from the high band. Black points are amplitudes on the short baseline between the two CARMA dishes. Red and green points are the SMT-CARMA baselines. Magenta and cyan points show the JCMT-CARMA baselines, and dark blue points are used for the SMT-JCMT baseline. Error bars show the *random* error only. *Bottom:* The same data after gain correction using the large scale model for M87 determined from data taken by the CARMA array. Gain-corrected SC and SD data are equal by definition.

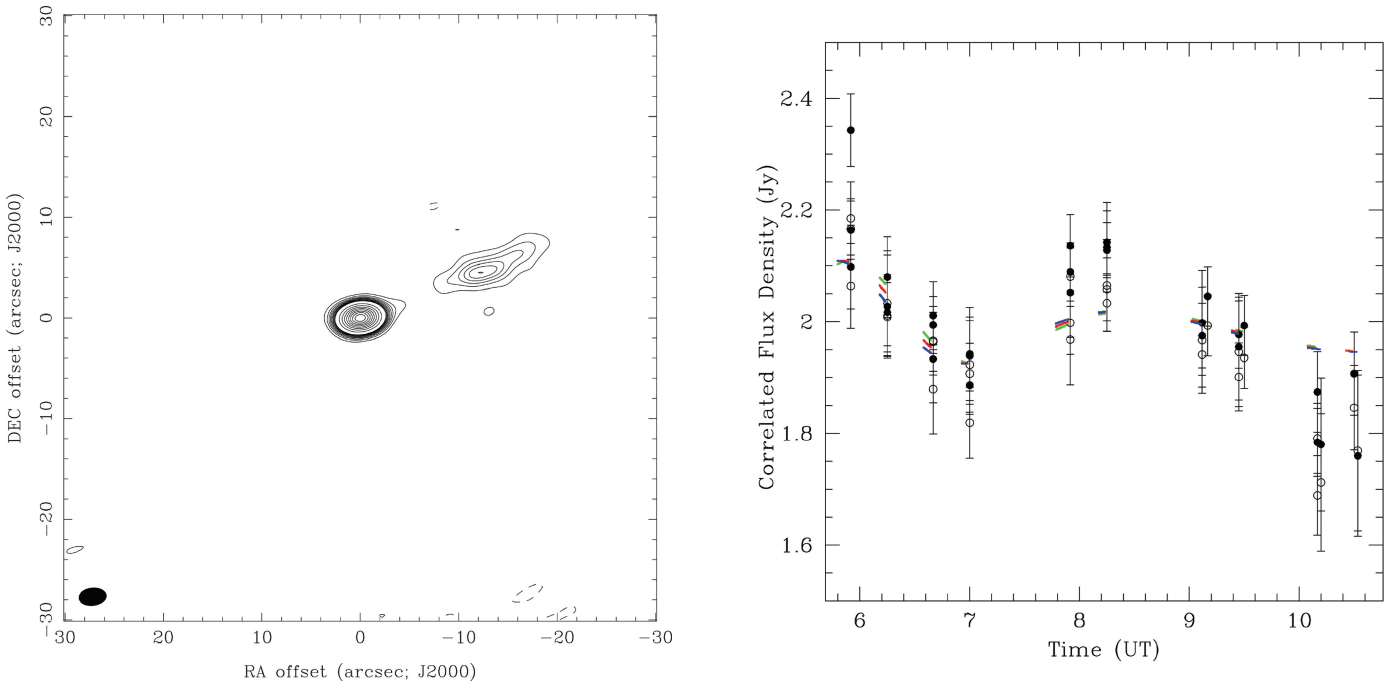

Fig S3. Left: An image of M87 on arcsecond scales made using data taken by the CARMA array during the 1.3mm VLBI observations. The well-known 'knot A' feature in the jet ~12 arcsec from the core is clearly detected. Contour levels (in units of 0.019 Jy/Beam): -3, -2, -1, 1, 2, 3, 4, 5, 6, 7, 8, 9, 10, 20, 30, 40, 50, 60, 70, 80, 90. Right: Plot of the VLBI visibility amplitudes after a-priori calibration, along with colored points showing visibilities at contemporaneous times derived from the source model. Corrections to the calibration of both CARMA antennas are derived by forcing the VLBI amplitudes to match the model. Green, red, and blue model points correspond to days 095, 096, and 097 respectively. Errors in the a-priori calibrated data are random errors added in quadrature to 5% errors due to a-priori calibration uncertainty.

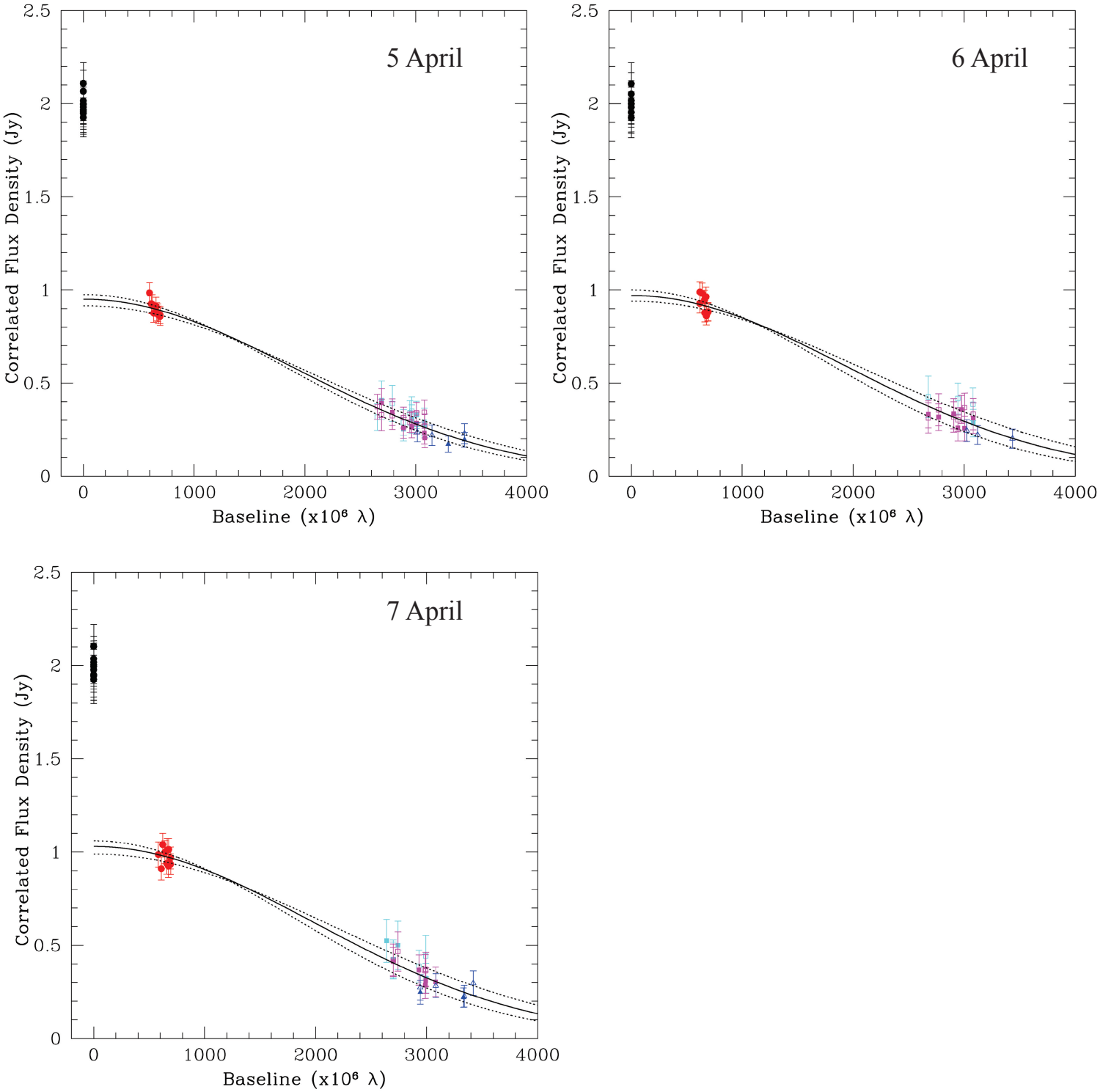

Fig S4. Stability of measured size for the M87 core over three consecutive days of observing. Plots of correlated flux density vs. baseline length for each of the three observing nights (2009 April 5, 6, 7 - left to right) are shown. Black points near zero-baseline length show flux density on the ~60m baseline between the two CARMA dishes, which we measure to be 2.0 Jy. The CARMA-SMT baselines are shown in red; the two baselines from CARMA dishes to the JCMT are shown in magenta and teal; the SMT-JCMT baseline is shown in blue. Calibration errors of 5% have been added in quadrature to the random errors associated with the incoherent fringe search performed on each baseline. Solid black curves show the linear least squares best-fit circular Gaussian models (see Table S1). Dotted lines show the circular Gaussian models corresponding to the 3σ limits on source size. Both the FWHM sizes and compact flux densities obtained from weighted least-squares fitting for each individual day are consistent at the 3σ level, indicating a constant compact structure at the jet launch point over the three day observing campaign.

Table S1. Circular Gaussian Fits to M87. Errors are 3σ

Day Number	Compact Flux Density (Jy)	Size FWHM (μas)
95	$0.95^{+0.06}_{-0.06}$	$40.3^{+2.5}_{-2.6}$
96	$0.97^{+0.07}_{-0.06}$	$39.8^{+3.8}_{-3.3}$
97	$1.03^{+0.05}_{-0.054}$	$39.1^{+3.5}_{-3.4}$
all days	$0.98^{+0.04}_{-0.04}$	$40.0^{+1.8}_{-1.8}$

Table S2. Detections of M87

Day	Time (UT)	Baseline	Band	u $(k\lambda)$	v $(k\lambda)$	Flux Density (Jy)	σ (Jy)
95	05:55	JC	low	2463469	980845	0.32	0.07
95	05:55	JD	low	2463470	980805	0.37	0.07
95	05:55	SC	high	-469518	396541	0.93	0.05
95	06:15	SC	high	-502735	387407	0.88	0.05
95	06:40	JC	high	2674795	1089740	0.25	0.06
95	06:40	JC	low	2674795	1089740	0.29	0.07
95	06:40	JD	high	2674802	1089700	0.26	0.06
95	06:40	JD	low	2674802	1089700	0.31	0.06
95	06:40	SC	high	-538819	375171	0.91	0.05
95	06:40	SJ	high	-3213615	-714569	0.17	0.04
95	07:00	JC	high	2735886	1140571	0.30	0.08
95	07:00	JC	low	2735886	1140571	0.35	0.08
95	07:00	JD	high	2735895	1140531	0.26	0.06
95	07:00	JD	low	2735895	1140531	0.29	0.06
95	07:00	SC	high	-563068	364819	0.88	0.05
95	07:55	JC	high	2795102	1284067	0.29	0.07
95	07:55	JD	high	2795117	1284028	0.23	0.06
95	07:55	JD	low	2795117	1284028	0.34	0.07
95	07:55	SC	high	-607095	334461	0.86	0.05
95	08:15	JC	high	2776588	1336411	0.27	0.06
95	08:15	JD	low	2776606	1336372	0.27	0.06
95	08:15	JD	high	2776606	1336372	0.20	0.05
95	08:15	SC	high	-614502	322984	0.86	0.05
95	09:10	JC	high	2617125	1476346	0.33	0.07
95	09:10	JC	low	2617125	1476346	0.33	0.06
95	09:10	JD	low	2617147	1476308	0.34	0.06
95	09:10	JD	high	2617147	1476308	0.28	0.06
95	09:10	SC	high	-610584	291201	0.87	0.05
95	09:10	SJ	high	-3227709	-1185145	0.20	0.04
95	09:10	SJ	low	-3227709	-1185145	0.23	0.05
95	09:30	JC	low	2520983	1524616	0.34	0.07
95	09:30	JD	low	2521007	1524579	0.29	0.05
95	09:30	SC	high	-600359	279824	0.88	0.05
95	10:10	JC	low	2271708	1614840	0.39	0.10

Table S2. Detections of M87

Day	Time (UT)	Baseline	Band	u $(k\lambda)$	v $(k\lambda)$	Flux Density (Jy)	σ (Jy)
95	10:10	JD	low	2271734	1614804	0.33	0.07
95	10:10	JD	high	2271734	1614804	0.34	0.07
95	10:10	SC	high	-566241	257863	0.92	0.05
95	10:10	SJ	low	-2837949	-1356978	0.22	0.05
95	10:30	JC	high	2120483	1656103	0.41	0.10
95	10:30	JD	low	2120510	1656067	0.33	0.08
95	10:30	JD	high	2120510	1656067	0.39	0.08
95	10:30	SC	high	-542608	247445	0.98	0.05
95	10:30	SJ	low	-2663091	-1408658	0.23	0.05
96	05:55	JC	low	2485873	989981	0.43	0.11
96	05:55	JD	low	2485875	989940	0.31	0.08
96	05:55	JD	high	2485875	989940	0.33	0.07
96	05:55	SC	high	-476340	394795	0.99	0.05
96	05:55	SJ	low	-2962214	-595186	0.24	0.06
96	06:15	SC	high	-508820	385540	0.98	0.06
96	06:40	JD	low	2688446	1099599	0.32	0.08
96	06:40	JD	high	2688446	1099599	0.34	0.08
96	06:40	SC	high	-543918	373173	0.95	0.05
96	07:00	JD	high	2745455	1150648	0.36	0.08
96	07:00	SC	high	-567334	362733	0.96	0.05
96	07:55	JC	low	2793149	1294382	0.39	0.09
96	07:55	SC	high	-608920	332216	0.88	0.05
96	08:15	JC	high	2770442	1346650	0.28	0.07
96	08:15	JD	low	2770460	1346611	0.33	0.08
96	08:15	JD	high	2770460	1346611	0.31	0.08
96	08:15	SC	high	-615407	320714	0.88	0.05
96	09:07	JD	high	2613108	1478596	0.26	0.07
96	09:07	JD	low	2613108	1478596	0.37	0.08
96	09:07	SC	high	-610211	290667	0.86	0.05
96	09:07	SJ	low	-3223296	-1187967	0.20	0.05
96	09:27	JC	low	2516027	1526820	0.42	0.08
96	09:27	JD	low	2516051	1526782	0.30	0.06
96	09:27	JD	high	2516051	1526782	0.26	0.07
96	09:27	SC	high	-599770	279299	0.88	0.05
96	10:10	JD	low	2243343	1623137	0.36	0.09
96	10:10	JD	high	2243343	1623137	0.32	0.07
96	10:10	SC	high	-561932	255780	0.93	0.05
96	10:10	SJ	low	-2805248	-1367394	0.22	0.05
97	05:55	JC	high	2507542	999197	0.42	0.10
97	05:55	JC	low	2507542	999197	0.42	0.10
97	05:55	JD	low	2507544	999157	0.42	0.09
97	05:55	JD	high	2507544	999157	0.41	0.08
97	05:55	SC	high	-483022	393024	1.04	0.06
97	06:15	SC	high	-514755	383650	1.00	0.06
97	06:40	SC	high	-548856	371156	1.01	0.06
97	06:40	SJ	high	-3250143	-738432	0.22	0.05
97	07:00	JD	high	2754202	1160800	0.29	0.07
97	07:00	JD	low	2754202	1160800	0.36	0.09
97	07:00	SC	high	-571431	360631	1.01	0.06
97	07:00	SJ	low	-3325623	-800209	0.30	0.07
97	07:55	JD	high	2790386	1304648	0.30	0.08
97	07:55	SC	high	-610566	329965	0.94	0.06

Table S2. Detections of M87

Day	Time (UT)	Baseline	Band	u $(k\lambda)$	v $(k\lambda)$	Flux Density (Jy)	σ (Jy)
97	08:15	SC	high	-616129	318441	0.97	0.06
97	09:07	JC	high	2595563	1488248	0.32	0.08
97	09:07	JC	low	2595563	1488248	0.44	0.11
97	09:07	JD	high	2595585	1488210	0.31	0.07
97	09:07	JD	low	2595585	1488210	0.37	0.09
97	09:07	SC	high	-608525	288417	0.93	0.06
97	09:27	JC	low	2494656	1536068	0.39	0.08
97	09:27	JD	high	2494680	1536031	0.37	0.08
97	09:27	SC	high	-597174	277090	0.94	0.06
97	09:27	SJ	low	-3091830	-1258978	0.23	0.06
97	10:12	JC	high	2199230	1635545	0.50	0.13
97	10:12	JD	low	2199257	1635509	0.47	0.11
97	10:12	SC	high	-555116	252670	0.91	0.06
97	10:12	SJ	low	-2754347	-1382876	0.28	0.06
97	10:32	JC	high	2039850	1675370	0.52	0.11
97	10:32	SC	high	-529411	242481	0.99	0.07
97	10:32	SJ	high	-2569261	-1432889	0.25	0.06
97	10:32	SJ	low	-2569261	-1432889	0.27	0.07

Note. — 1.3mm VLBI detections of M87 in April 2009. Scans are referred to by day of year, UT start time, baseline, and observing band. The projections of the baseline length east and north in the direction of M87 as measured in units of thousands of wavelengths are indicated as u and v. The error on the detected flux density includes a 5% systematic component added in quadrature to the random error.

References and Notes

1. D. Richstone *et al*., Supermassive black holes and the evolution of galaxies. *Nature* **395**, A14 (1998).

2. D. L. Meier, S. Koide, Y. Uchida, Magnetohydrodynamic production of relativistic jets. *Science* **291**, 84 (2001). doi:10.1126/science.291.5501.84 Medline

3. R. D. Blandford, R. L. Znajek, Electromagnetic extraction of energy from Kerr black holes. *Mon. Not. R. Astron. Soc.* **179**, 433 (1977).

4. R. D. Blandford, D. G. Payne, Hydromagnetic flows from accretion discs and the production of radio jets. *Mon. Not. R. Astron. Soc.* **199**, 883 (1982).

5. J.-P. De Villiers, J. F. Hawley, J. H. Krolik, S. Hirose, Magnetically driven accretion in the Kerr metric. III. unbound outflows. *Astrophys. J.* **620**, 878 (2005). doi:10.1086/427142

6. J. McKinney, General relativistic magnetohydrodynamic simulations of the jet formation and large-scale propagation from black hole accretion systems. *Mon. Not. R. Astron. Soc.* **368**, 1561 (2006). doi:10.1111/j.1365-2966.2006.10256.x

7. D. Garofalo, D. A. Evans, R. M. Sambruna, The evolution of radio-loud active galactic nuclei as a function of black hole spin. *Mon. Not. R. Astron. Soc.* **406**, 975 (2010).

8. A. Tchekhovskoy, J. McKinney, Prograde and retrograde black holes: whose jet is more powerful? *Mon. Not. R. Astron. Soc.*, arXiv1201.4385 (2012).

9. D. Clery, Astronomy. Worldwide telescope aims to look into Milky Way galaxy's black heart. *Science* **335**, 391 (2012). doi:10.1126/science.335.6067.391 Medline

10. J. Blakeslee *et al*.; The ACS Fornax Cluster Survey, V. Measurement and Recalibration of Surface Brightness Fluctuations and a Precise Value of the Fornax-Virgo Relative Distance. *Astrophys. J.* **694**, 556 (2009). doi:10.1088/0004-637X/694/1/556

11. K. Gebhardt *et al*., The black hole mass in M87 from Gemini/NIFS adaptive optics observations. *Astrophys. J.* **729**, 119 (2011). doi:10.1088/0004-637X/729/2/119

12. J. A. Biretta, F. Zhou, F. N. Owen, Detection of proper motions in the M87 jet. *Astrophys. J.* **447**, 582 (1995). doi:10.1086/175901

13. E. S. Perlman, J. A. Biretta, W. B. Sparks, F. D. Macchetto, J. P. Leahy, the optical-near-infrared spectrum of the M87 jet from hubble space telescope observations. *Astrophys. J.* **551**, 206 (2001). doi:10.1086/320052

14. H. L. Marshall *et al*., A high-resolution X-ray image of the jet in M87. *Astrophys. J.* **564**, 683 (2002). doi:10.1086/324396

15. W. Junor, J. A. Biretta, M. Livio, Formation of the radio jet in M87 at 100 Schwarzschild radii from the central black hole. *Nature* **401**, 891 (1999). doi:10.1038/44780

16. T. P. Krichbaum *et al*., Sub-milliarcsecond imaging of Sgr A* and M 87. *J. Phys. Conf. Ser.* **54**, 328 (2006).

17. C. Ly, R. C. Walker, W. Junor, High-frequency VLBI imaging of the jet base of M87. *Astrophys. J.* **660**, 200 (2007). doi:10.1086/512846

18. Y. Y. Kovalev, M. L. Lister, D. C. Homan, K. I. Kellermann, The inner jet of the radio galaxy M87. *Astrophys. J.* **668**, L27 (2007). doi:10.1086/522603

19. K. Asada, M. Nakamura, The structure of the M87 jet: A transition from parabolic to conical streamlines. *Astrophys. J.* **745**, L28 (2012). doi:10.1088/2041-8205/745/2/L28

20. See the supplementary materials on *Science* Online.

21. J. C. McKinney, R. D. Blandford, Stability of relativistic jets from rotating, accreting black holes via fully three-dimensional magnetohydrodynamic simulations. *Mon. Not. R. Astron. Soc.* **394**, L126 (2009). doi:10.1111/j.1745-3933.2009.00625.x

22. J. Gracia, N. Vlahakis, I. Agudo, K. Tsinganos, S. V. Bogovalov, synthetic synchrotron emission maps from MHD models for the jet of M87. *Astrophys. J.* **695**, 503 (2009). doi:10.1088/0004-637X/695/1/503

23. K. Hada *et al*., An origin of the radio jet in M87 at the location of the central black hole. *Nature* **477**, 185 (2011). doi:10.1038/nature10387 Medline

24. A. P. Marscher *et al*., The inner jet of an active galactic nucleus as revealed by a radio-to-gamma-ray outburst. *Nature* **452**, 966 (2008). doi:10.1038/nature06895 Medline

25. A. E. Broderick, A. Loeb, Imaging the black hole silhouette of M87: Implications for jet formation and Black Hole spin. *Astrophys. J.* **697**, 1164 (2009). doi:10.1088/0004-637X/697/2/1164

26. P. E. Hardee, Stability properties of strongly magnetized spine-sheath relativistic jets. *Astrophys. J.* **664**, 26 (2007). doi:10.1086/518409

27. C. P. Fragile, Effective inner radius of tilted black hole accretion disks. *Astrophys. J.* **706**, L246 (2009). doi:10.1088/0004-637X/706/2/L246

28. A. Broderick, A. Loeb, R. Narayan, The event horizon of Sagittarius A*. *Astrophys. J.* **701**, 1357 (2009). doi:10.1088/0004-637X/701/2/1357

29. J. M. Bardeen, J. A. Petterson, The lense-thirring effect and accretion disks around Kerr black holes. *Astrophys. J.* **195**, L65 (1975). doi:10.1086/181711

30. C. Gammie, S. Shapiro, J. McKinney, Black hole spin evolution. *Astrophys. J.* **602**, 312 (2004). doi:10.1086/380996

31. J. Dexter, J. C. McKinney, E. Agol, The size of the jet launching region in M87. *Mon. Not. R. Astron. Soc.* **421**, 1517 (2012). doi:10.1111/j.1365-2966.2012.20409.x

32. H. Falcke, F. Melia, E. Agol, Viewing the shadow of the black hole at the Galactic center. *Astrophys. J.* **528**, L13 (2000). doi:10.1086/312423 Medline

33. T. Johannsen, D. Psaltis, Testing the no-hair theorem with observations in the electromagnetic spectrum. II. Black hole images. *Astrophys. J.* **718**, 446 (2010). doi:10.1088/0004-637X/718/1/446

34. J. A. Biretta, W. Junor, M. Livio, Evidence for initial jet formation by an accretion disk in the radio galaxy M87. *New Astron. Rev.* **46**, 239 (2002). doi:10.1016/S1387-6473(01)00188-9

35. A. E. Broderick, R. Blandford, Covariant magnetoionic theory – I. Ray propagation. *Mon. Not. R. Astron. Soc.* **342**, 1280 (2003). doi:10.1046/j.1365-8711.2003.06618.x

36. A. E. Broderick, A. Loeb, Imaging optically-thin hotspots near the black hole horizon of Sgr A* at radio and near-infrared wavelengths. *Mon. Not. R. Astron. Soc.* **367**, 905 (2006). doi:10.1111/j.1365-2966.2006.10152.x

37. V. L. Fish *et al*., 1.3 mm wavelength VLBI of Sagittarius A*: Detection of time-variable emission on event horizon scales. *Astrophys. J.* **727**, L36 (2011). doi:10.1088/2041-8205/727/2/L36

38. S. S. Doeleman *et al*., Structure of Sagittarius A* at 86 GHZ using VLBI closure quantities. *Astron. J.* **121**, 2610 (2001). doi:10.1086/320376

39. S. S. Doeleman *et al*., Event-horizon-scale structure in the supermassive black hole candidate at the Galactic Centre. *Nature* **455**, 78 (2008). doi:10.1038/nature07245 Medline

40. A. E. E. Rogers, S. S. Doeleman, J. M. Moran, Fringe detection methods for very long baseline arrays. *Astron. J.* **109**, 1391 (1995). doi:10.1086/117371

41. J. M. Bardeen, W. H. Press, S. A. Teukolsky, Rotating black holes: Locally nonrotating frames, energy extraction, and scalar synchrotron radiation. *Astrophys. J.* **178**, 347 (1972). doi:10.1086/151796